Boosting hydrogen production at room temperature by synergizing theory and experimentation

Kavita Thakkar,[†,‡] Abhinav Bajpai,[¶] Sushant Kumar,[*,¶] and Kavita Joshi[*,†,‡]

†*Physical and Materials Chemistry Division, CSIR-National Chemical Laboratory, Dr. Homi Bhabha Road, Pashan, Pune-411008, India*

‡*Academy of Scientific and Innovative Research (AcSIR), Sector 19, Kamla Nehru Nagar, Ghaziabad, Uttar Pradesh-201002, India*

¶*Gas-Solid Interaction Laboratory, Department of Chemical and Biochemical Engineering, Indian Institute of Technology Patna, Bihta, Patna-801106, Bihar, India*

E-mail: sushantkumar@iitp.ac.in; k.joshi@ncl.res.in

Abstract

Methane is a major constituent of natural gas and is widely used in hydrogen production. However, its high symmetry poses a challenge, as breaking the strong C-H bond requires substantial energy input. Hence, there is a pressing need to develop efficient catalysts for methane conversion. By synergizing theory and experimentation, the search for a better catalyst can be accelerated, potentially boosting methane conversion processes. In the present work, theoretical findings prompted the experiments, which revealed the spontaneous dissociation of CH_4 on selected facets of β-Ga_2O_3. Additionally, the activation barrier for ethane formation was merely 0.1 eV. NTP-assisted conversion of methane in the presence of β-Ga_2O_3 confirmed these findings. The formation rate of hydrogen and ethane rises to 366 μmolg^{-1}h^{-1} and 86.62 μmolg^{-1}h^{-1},

respectively, in the presence of β-Ga_2O_3, in contrast to 281.4 $\mu molg^{-1}h^{-1}$ and 66 $\mu molg^{-1}h^{-1}$ without catalysts. For the CH_4-H_2O reaction in the presence of β-Ga_2O_3, there is an increase of 74.42% in the CO formation rate compared to the reaction without the catalyst. An electronic structure analysis revealed that electrophilic oxygen species on the β-Ga_2O_3 (-202) surface play a vital role in the decomposition of methane, facilitating C-H bond cleavage.

Introduction

Methane is a principal component of natural gas, and its conversion to value-added chemicals is a crucial area of investigation owing to its potential for reducing dependence on fossil fuels and mitigating greenhouse gas emissions. However, methane's high stability and low reactivity significantly challenge its transformation.[1] One promising approach for activating methane is through heterogeneous catalysis, which promotes breaking the C-H bond.[2–6] Methane conversion produces hydrogen in addition to carbon monoxide, hydrocarbons, or

Table 1: We report different methods for H_2 production from methane, reactions, catalysts, reaction temperature.

Process	**Reaction**	**Catalysts**	**Reaction temperature (°C)**
Steam reforming of methane[7,8]	1) $CH_4 + 2H_2O \rightarrow CO_2 + 4H_2$ 2) $CH_4 + H_2O \rightarrow CO + 3H_2$	Ni/Al_2O_3, Ni/MgO, Ni-CeO_2-Al_2O_3, Ni-CeO_2-ZrO_2-SiO_2, $Ni/MgAl_2O_4$, Ru-CaO/$Ca_3Al_2O_6$	500 - 800
Dry reforming of methane[9,10]	$CH_4 + CO_2 \rightarrow 2CO + 2H_2$	Rh/MgO, Rh/γAl_2O_3, Ni-MgO-CeO_2, Ni-MgO-Al_2O_3, $Ni/MgAl_2O_4$, Ni-Fe/MgAlO, Ni/SiO_2	400 - 800
Partial oxidation of methane[11]	$CH_4 + 1/2\ O_2 \rightarrow CO + 2H_2$	RuO_2, Ni/MgO, Au-Pd/TiO_2, $NiAl_2O_4$, Pt-CeO_2, $Ni_{0.5}WO_x/Al_2O_3$, $BaFe_3Al_9O_{19}$, $La_{0.8}Sr_{0.2}FeO_3$, $LaFeO_3$	600 - 900
Non-oxidative coupling of methane[12]	$2CH_4 \rightarrow C_2H_6 + H_2$	Pt/CeO_2, Pd/αAl_2O_3, Fe/SiO_2, Ta/SiO_2, Fe@SiO_2, Fe/HZSM-5, Pt/Mo_2TiC_2	250 - 1000
Catalytic decomposition of methane[13]	$CH_4 \rightarrow C + 2H_2$	Co/Ce-TiO_2, Co/MgO, Fe/Al_2O_3, Fe/CeO_2, Ni-CeO_2/ SiO_2, Ni/TiO_2, Co/SiO_2	500 - 800

alcohols, which are essential building blocks of the chemical industry. There are different

routes to convert methane to hydrogen, including steam reforming of methane (SRM),[7,8] dry reforming of methane (DRM),[9,10] partial oxidation of methane (POM),[11] non-oxidative coupling of methane (NOCM),[12] and catalytic decomposition of methane (CDM).[13] Table 1 summarizes the catalysts and reaction temperatures used in these methods. Further details could be found in the respective references. At present, steam reforming of methane is the most preferred commercial method for producing hydrogen with minimum carbon dioxide emissions, compared to dry reforming and partial oxidation of methane. SRM is highly endothermic and results in an H_2:CO ratio of 3:1.[7] Ni-based catalysts with promoters are widely used in industry for methane steam reforming.[14] However, the coke formation and sintering are major drawbacks for Ni-based catalysts. Even though CDM is cheaper and produces less CO_2 emissions compared to SRM, it faces challenges such as regenerating catalysts and deactivation caused by carbon encapsulation, which limits its use in industry.[15] Moreover, the thermo-catalytic conversion of methane requires high operating temperatures to cleave the C-H bond (as reported in Table 1). On the other hand, photocatalytic conversion can be achieved under mild operating conditions and has gained increasing attention.[16] Various experiments have been conducted on numerous photocatalysts to reform methane into valuable products.[17,18] However, they suffer from several limitations, such as low usage of visible light, rapid recombination of charge carriers, and limited migration ability of electrons and holes. These limitations hinder their industrial application. Consequently, there is a need for new methods for methane conversion.

Non-thermal plasma (NTP) has gained attention for its ability to activate reactions at low temperatures by generating energetic radicals and electrons, making it an attractive option for methane conversion.[19,20] Several studies have investigated the use of NTP for methane conversion.[21–24] The results of these studies have demonstrated that NTP can effectively convert methane to hydrogen and carbon monoxide in the presence of water, albeit with varying levels of selectivity and conversion efficiency. Combining catalysis with NTP has recently become popular due to enhanced selectivity towards desirable products.[25–27]

Our recent work demonstrates that NTP catalysis is a promising approach for CO_2-H_2O conversion and ammonia synthesis.[28,29] Chung *et al.* showed that the combined effect of plasma and $LaFeO_3$ photocatalyst enhances syngas formation rate by 42%.[30] It is attributed to the surface modifications promoted by plasma, which increases the lifetime of charge carriers. Meng *et al.* investigated Ga-UZSM-5 photocatalysts for conversion of natural gas to gasoline near ambient conditions.[20] They observed that the reaction could not proceed without plasma, and no products were formed. However, when plasma was combined with these photocatalysts, the C_6-C_9 hydrocarbons are formed. Moreover, incorporating TiO_2 further enhances the conversion rate from 37.9 % to 58.4 %. This enhancement in reactivity is attributed to the utilization of UV light generated in plasma. However, despite these advances, significant efforts are still required to make NTP catalysis viable for large-scale applications.

Density functional theory (DFT) has emerged as a valuable tool for optimizing and designing high-performance catalysts aimed at enhancing methane conversion.[31–33] For instance, DFT study was first to report that $IrO_2(110)$ is highly reactive toward methane,[34] later confirmed by experiments showing methane dissociation at low temperatures on $IrO_2(110)$ surfaces.[35] Kwon *et al.* demonstrated that methane can directly oxidize to ethane on a highly oxidized Pd/CeO_2 catalyst.[36] DFT study highlight the advantages of Pd-O-Pd for C-C coupling and Pd-O-Ce for CH_4 dehydrogenation. Liu *et al.* synthesized sulfided Fe_3O_4 catalysts displaying high selectivity towards ethylene.[37] DFT analysis revealed that sulphur sites play a crucial role in C-H bond cleavage, leading to the formation of C_2H_4. These investigations emphasize the potential of synergizing DFT with experimental approaches to rationally design efficient catalysts.

Ga_2O_3 has shown promising results for photocatalytic conversion of methane to hydrogen and ethane near room temperature. However, its activity is limited by adsorption under the UV region and fast recombination of charge carriers.[38–42] In the present study, we investigate the reactivity of β-Ga_2O_3 by employing DFT and discovered that the reactivity is facet-

dependent. Specifically, the β-Ga_2O_3 (-202) facet exhibits high activity and promotes the spontaneous dissociation of methane. Additionally, we observed a minimum barrier for ethane formation compared to other catalysts investigated in theory[43–45] (discussed further in the Results and Discussion section). Further, the NTP-assisted conversion of methane in the presence of β-Ga_2O_3 supports these results by revealing that β-Ga_2O_3 enhances selectivity towards hydrogen and ethane. We delve into the electronic properties of β-Ga_2O_3 to explain the observed reactivity.

Computational Details

All the calculations are carried out within the Kohn-Sham formalism of DFT. Projector Augmented Wave potential[46] is used, with Perdew Burke Ernzerhof (PBE) approximation for the exchange-correlation and generalized gradient approximation,[47] as implemented in plane wave, pseudo-potential based code, Vienna Ab initio Simulation Package (*VASP*).[48] To account for the dispersion effect, Van der Waals interactions are applied as implemented in the Grimme approach (DFT-D2).[49] Bulk of monoclinic β-Ga_2O_3 is taken from the materials project.[50] The calculated lattice parameters are a= 12.56 Å, b= 3.02 Å, and c= 5.85 Å, which agrees well with the experimentally reported ones, a= 12.23 Å, b= 3.04 Å, and c= 5.80 Å.[51] A slab of 3x1 and 2x1 with 3 layers is cleaved in (-202) and (111) direction, respectively, using VNL,[52] with the bottom layer fixed to imitate the bulk configuration. Monkhorst-Pack grid of 3x2x1 and 2x2x1 is used to sample the (-202) and (111) surfaces, resulting in 2 k-points in the IBZ. A vacuum of 20.0 Å is sufficient to avoid interaction between adjacent images along the z-direction. Spin-polarized geometry optimization is performed with a force cutoff of 0.05 eV/Å on the unfixed ions. The total energies are converged below 10^{-4} eV for each SCF cycle. Adsorption energy (E_{ads}) is calculated using the formula: $E_{ads} = E_{system} - [E_{surface} + E_{adsorbate}]$. Here, E_{system} corresponds to energy of the entire system (surface + adsorbate), $E_{surface}$ is the energy of bare β-Ga_2O_3 surface, and $E_{adsorbate}$ is the

energy of the adsorbate molecule. Further, Activation barrier (E_a) is determined by using Climbing Image-Nudged Elastic Band (CI-NEB) method,[53] with 3 images and a force cutoff of 0.1 eV/Å. To understand the surface reactivity, we calculate the site-specific projected density of states (*pDOS*) and Mulliken charges with a denser k-mesh using LOBSTER.[54]

Experimental procedure

A co-axial cylindrical di-electric barrier discharge plasma (DBD) reactor is used to convert CH_4 and CH_4-H_2O in presence of gallium oxide into value added products. The DBD reactor is designed using two quartz tubes that are concentric. The outer tube's inner diameter (ID) and outer diameter (OD) were 25 mm and 28 mm, respectively, while the inner tube had 18 mm ID and 20 mm OD. This configuration resulted in a discharge gap of 2.5 mm. A stainless steel mesh with a length of 140 mm is wrapped around the outer tube as a grounded electrode, and a stainless steel rod is put inside the inner tube as a high voltage electrode. The discharge length of the DBD reactor is defined as the length of the grounded electrode i.e. 140 mm. Plasma generator supplied by Arshad Electronics Pvt. Ltd., Mumbai, India is used to generate the DBD discharge using AC current that is controlled to produce high voltages of 10-15 kV at 50 Hz. To regulate the flow of methane gas, a rotameter (Aalborg, USA) is utilized, and methane is introduced into the DBD reactor at a flow rate of 30 ml/min. The conversion of CH_4 and CH_4-H_2O is carried out by simply placing 0.8 g of β-Ga_2O_3 (Sigma Aldrich) between glass wool and quartz beads. At specific energy input of 17.2 J/L, non-thermal plasma is incorporated for 8 minutes for every run of experiments. The system filled with 1.5 ml of water for CH_4-H_2O conversion both with and without a catalyst. The initial and final gas concentrations are measured with a carbo-sieve column using a GC-5800 gas chromatograph (Centurion Scientific, India). A flame ignition detector (FID) is used to monitor the amount of hydrocarbons produced during the reactions, and a thermal conductivity detector (TCD) is used to measure the amounts of CH_4, CO, and H_2.

The conversion, yield, and selectivity of the products are measured using the formulae:

$$CH_4 \text{ Conversion}(\%) = [\frac{(\text{Inlet concentration of } CH_4 \text{ - Outlet concentration of } CH_4)}{\text{Inlet concentration of } CH_4}] \times 100$$

$$\text{Products yield}(\%) = [\frac{\text{Concentration of formed products}}{\text{Inlet concentration of } CH_4}] \times 100$$

$$H_2 \text{ selectivity}(\%) = [\frac{\text{Concentration of formed } H_2}{2\times(\text{Inlet concentration of } CH_4 \text{ - Outlet concentration of } CH_4)}] \times 100$$

$$CO \text{ selectivity}(\%) = [\frac{\text{Concentration of formed CO}}{(\text{Inlet concentration of } CH_4 \text{ - Outlet concentration of } CH_4)}] \times 100$$

$$C_2H_6,\ C_2H_4,\ C_2H_2 \text{ selectivity}(\%) = [\frac{2\times(\text{Concentration of formed } C_2H_6,\ C_2H_4,\ C_2H_2)}{(\text{Inlet concentration of } CH_4 \text{ - Outlet concentration of } CH_4)}] \times 100$$

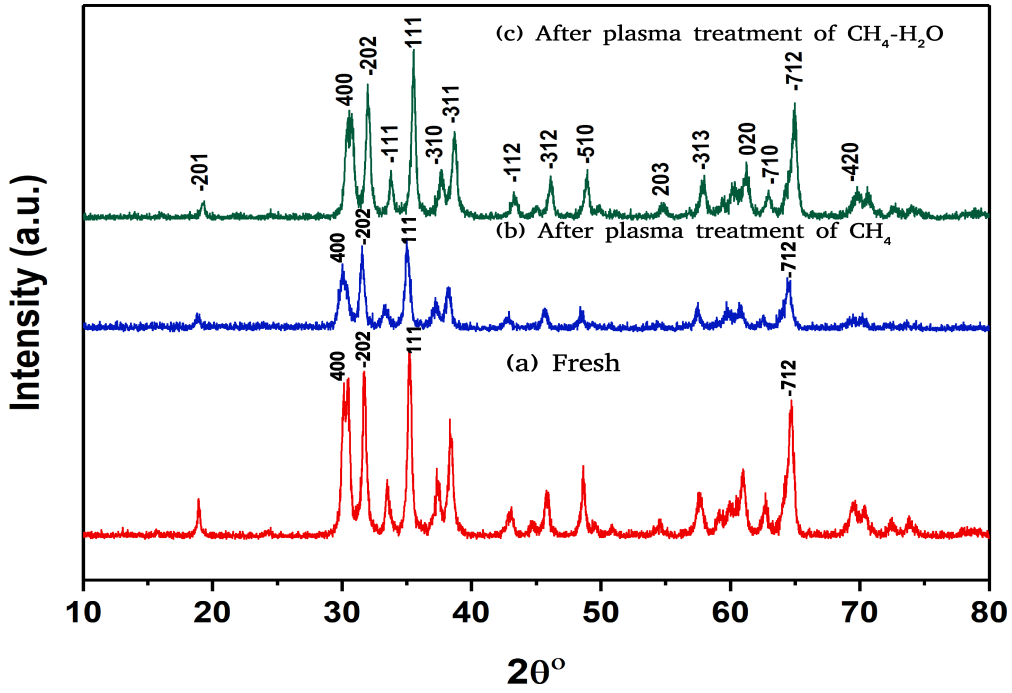

Figure 1: X-ray diffraction for β-Ga_2O_3 (a) Fresh, (b) after plasma treatment of CH_4, and (c) after plasma treatment of CH_4-H_2O. JCPDS #00-041-1103.

Characterization of catalysts

Using a Rigaku X-ray diffractometer with Cu Kα radiation flux (λ= 1.518 Å), the X-ray diffraction (XRD) pattern for freshly prepared and spent catalysts is recorded in Figure 1. The working voltage of the diffractometer is 10 kV, and the corresponding scan rate is $2^{\circ}min^{-1}$ for 2θ value range from 20° to 90°. The nitrogen adsorption/desorption isotherms and Brunauer-Emmett-Teller (BET) surface area are estimated at -196 °C using a Micrometrics, 3 FLEX equipment. For the analysis, β-Ga_2O_3 is first degassed at 200 °C for 4

hours in an N_2 atmosphere to remove moisture content and any surface-adsorbed impurities. Using the same instrument as for BET measurement, the β-Ga_2O_3 sample is also tested for carbon dioxide temperature programmed desorption (CO_2- TPD). CO_2-TPD was performed to investigate the surface properties of β-Ga_2O_3. The fresh catalyst is first degassed for CO_2-TPD for one hour at 400 °C in a helium atmosphere. The temperature is then lowered to 50 °C to allow CO_2 to adsorb on the catalyst surface. Subsequently, desorption of CO_2 is examined at a ramp rate of 10 °C min^{-1} between 50-800 °C.

Results and discussion

Ga_2O_3 is known to exists in various phases viz. α, β, γ, δ, and ϵ of which β-Ga_2O_3 is most stable under normal temperature and pressure conditions.[55] Unit cell of β-Ga_2O_3 consist of two kinds of Ga^{3+} and three distinct O^{2-} ions, as illustrated in Figure SI-1. Ga(I) and Ga(II) have octahedral and tetrahedral coordination, respectively. O(I) has tetrahedral coordination and is connected to three Ga atoms of the octahedral unit and one of the tetrahedral unit. O(II) is coordinated to three Ga atoms, of which two belongs to the octahedral and one belongs to the tetrahedral chain and O(III) is coordinated with two tetrahedral Ga atoms and one octahedral Ga atom. The XRD pattern shown in Figure 1 illustrated the presence of a monoclinic structured β-Ga_2O_3 phase, JCPDS #00-041-1103.[56] Although the spent catalyst showed a decrease in the intensity of peaks, the phase of gallium oxide did not change during the reaction. Furthermore, BET surface area is calculated to be 37.22 m^2/g for β-Ga_2O_3 sample. As illustrated in Figure SI-2, the isotherm corresponds to type IV with H3 hysteresis loops, concluding the presence of slit-like pores and mesoporous nature of catalyst.[57]

First, we investigated the interaction of methane with the prominent peaks observed from XRD corresponding to the (111) and (-202) planes. In Figure SI-3(a) and SI-4(a), we report β-Ga_2O_3 (111) and (-202) surfaces with unique adsorption sites marked. CH_4 is found

to weakly interact or physisorb on β-Ga_2O_3 (111) surface. The final adsorption positions on β-Ga_2O_3 (111) are noted in Figure SI-3(b). It is observed that for two out of 14 cases, methane is weakly adsorbed over β-Ga_2O_3 (111). The C-H bond is slightly elongated to 1.11 Å compared to molecular CH_4 (1.09 Å) and E_{ads} = -0.49 eV. A representative geometry is shown in Figure SI-3(c). For physisorption of methane on β-Ga_2O_3 (111) the E_{ads} are in the range of -0.32 eV to -0.07 eV and the distance between surface oxygen and hydrogen of CH_4 is >2.5 Å. Interestingly, on the β-Ga_2O_3 (-202) facet, when CH_4 is placed at sites 1, 2, and 3 (refer to Figure SI-4(a)), it undergoes spontaneous dissociation. Regardless of the initial placement (i.e. site 1, 2, or 3), the fragmented H/CH_3 adsorb onto the bi-coordinated oxygen site, as depicted in Figure SI-4(b). However, at sites 4 - 10, as indicated in Figure SI-4(a), physisorption is observed and final adsorption sites are noted in Figure SI-4(b). It should be noted that the species formed upon interaction of methane with the catalysts are henceforth denoted with an asterisk (*). As shown in Figure 2(a and b), the fragmented CH_3* either adsorbs on top of surface oxygen (O_s) to from methoxy (CH_3O_s*) or remains as a free methyl species (CH_3*) and the H* binds to the oxygen with an O_s-H bond length of 0.98 Å. As evident from Table 2, the formation of CH_3O_s* is thermodynamically more favorable over CH_3*. Additionally, physisorption is observed to occur at O_s-H distance

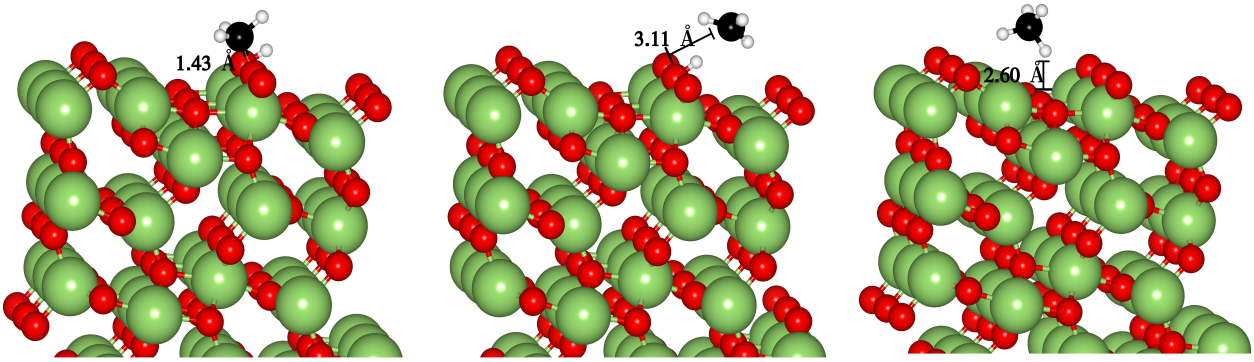

Figure 2: Optimized geometries for CH_4 interaction with β-Ga_2O_3 (-202). (a) Dissociation of CH_4 to CH_3O_s* and H* adsorbed on adjacent surface oxygens, (b) dissociation of CH_4 to form free CH_3* species and H* binds to surface O and, (c) Physisorption of CH_4. Asterisk (*) donates an activated species formed by interaction of CH_4 with the surface.

of $\geq$ 2.6 Å , with E_{ads} typically lying in the range of -0.41 eV to -0.12 eV (refer Table

Table 2: We report shortest bond distance between surface oxygen (O_s) and C/H of methane molecule and adsorption energy (E_{ads}). C-H bond is ∼1.10 Å for all cases reported below. Asterisk (*) donates an activated species.

Class	**O_s-C (Å)**	**O_s-H (Å)**	**E_{ads} (eV)**	**No. of cases**
methoxy (CH_3O_s*)	1.43	0.98	-4.82	1
methyl (CH_3*)	3.11/3.01	0.98/0.99	-1.03/-0.98	2
physisorbed	>3.0	2.5 to 2.7	-0.41 to -0.12	8

2). A representative geometry for physisorption is shown in Figure 2-(c). Chaudhari *et al.* investigated (001) facet of β-Ga_2O_3, and their findings show that a barrier of 0.65 eV is required to break the first C-H bond of methane.[58] Interestingly, we observed spontaneous dehydrogenation of CH_4 on β-Ga_2O_3 (-202); the underlying reactivity of (-202) could be understood by analyzing the electronic structure which we will discuss in detail later.

Next, we investigate the co-adsorption of two CH_4 molecules on β-Ga_2O_3 (-202). For the co-adsorption of two molecules, we considered a 4x1 super cell with three layers (240 atom system), and the bottom layer is fixed to bulk configuration. In the initial configuration one of the CH_4 is placed at site 1 shown in Figure SI-4(a) and the second molecule is placed at five sites in it's vicinity. Distinct adsorption configurations are observed, such as (i) the dissociation of both molecules to form CH_3O_s* and CH_3* species, (ii) the conversion of both methane to methyl species, (iii) the dissociation of one CH_4 molecule to form CH_3* while the other undergoes physisorption, and (iv) physisorption of both CH_4 molecules. Schematic representation of the observed geometries along with corresponding E_{ads} can be found Figure SI-5(a-d). With E_{ads} of -5.58 eV, the formation of CH_3O_s* and CH_3* species is thermodynamically most stable.

The spontaneous dissociation of CH_4 into surface adsorbed or free CH_3* during co-adsorption can help accelerate the reaction. We investigated the barrier required for non-oxidative coupling of methane using CI-NEB. Considering the thermodynamically most favored geometry obtained by co-adsorbing two molecules of methane as the initial state, we determined the activation barrier for formation of ethane over β-Ga_2O_3 (-202). In Figure

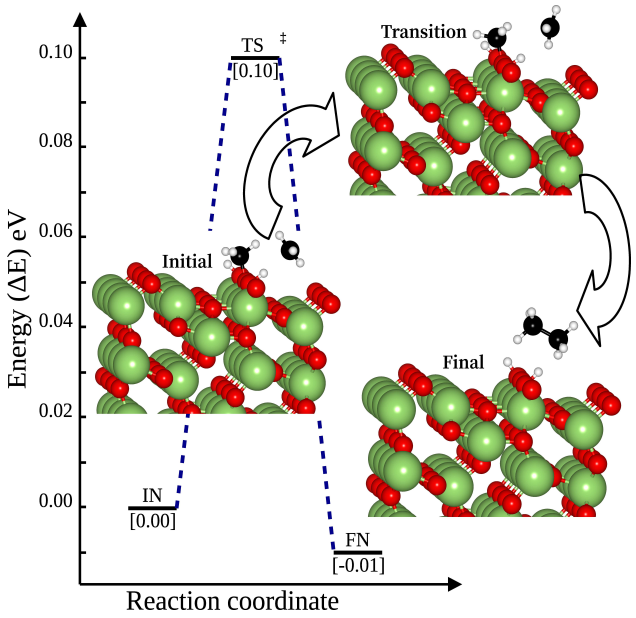

Figure 3: Energy profile for formation of C_2H_6. Activation barrier is calculated to be 0.1 eV. Formed ethane molecule is found to desorb from the surface. IN= initial state, TS= transition state, and FN= final state.

3 we report the reaction pathway along with a schematic representation of the initial (IN), transition (TS), and Final (FN) state. Within our framework, the barrier of CH_3-CH_3

Table 3: We compare the activation barrier for CH_3-CH_3 coupling with the existing literature. The activation barrier are computed through DFT calculations. Here, e = experimental and d = dft study.

Catalysts	**$CH_3 + CH_3 \rightarrow C_2H_6$** E_a **(eV)**	**Reference**
β-Ga_2O_3 (-202)	0.1	current work
Pd/CeO_2 (111) $^{e+d}$	0.28	[36]
$Pt_1/Ce_{1-x}Pt_xO_{2-\delta}$ (111) ^{d}	1.54	[43]
$Pt_3/Ce_{1-x}Pt_xO_{2-\delta}$ (111)	1.08	
$Pt_{10}/Ce_{1-x}Pt_xO_{2-\delta}$ (111)	1.17	
Pd_1TiO_2 (001) $^{e+d}$	1.74	[44]
Mo_4C_2/ZSM-5 ^{d}	1.28	[45]

coupling turns out to be 0.1 eV. The reaction is exothermic as the product here, C_2H_6 is slightly more favorable than the reactant. Additionally, the formed ethane desorbs from the surface, the distance of carbon atom being 3.31 Å from the surface. Moreover, the C-C bond length is 1.53 Å, which is the same as that of molecular ethane. Table 3 compares the activation barriers investigated through DFT for the coupling of CH_3-CH_3 in the current

work to those reported previously. As shown in Table 3, β-Ga_2O_3(-202) not only results in the spontaneous dissociation of methane but also significantly decreases the barrier for converting CH_4 to C_2H_6.

Table 4: We report the bond lengths and E_{ads} for co-adsorbed CH_4 and H_2O. Os-C(Mt) is the distance between surface oxygen and carbon of methane and Os-H(Mt) is the distance between surface oxygen and hydrogen of methane. Ga-O(Wt) is the distance between surface Ga and oxygen of H_2O. O-H1(Wt) and O-H2(Wt) are the O-H bond lengths of water, and ∠HOH is the bond angle of H_2O. All the geometries are tabulated in the decreasing order of adsorption energy E_{ads}. Here, O_s = surface oxygen, Mt = methane, and Wt = water

co-adsorption of CH_4 and H_2O							
Geometry	**O_s-C(Mt) (Å)**	**O_s-H(Mt) (Å)**	**Ga-O(Wt) (Å)**	**O-H1(Wt) (Å)**	**O-H2(Wt) (Å)**	**∠HOH(Wt) (°)**	**E_{ads} (eV)**
1	1.43	0.97	2.14	0.98	0.99	109.8	-5.76
2	1.43	0.98	2.15	0.98	0.99	110.8	-5.75
3	1.44	0.98	4.00	0.97	1.01	104.3	-5.34
4	1.45	0.97	3.63	0.98	0.98	103.4	-5.19
5	3.13	0.98	2.31	0.97	1.00	113.2	-2.04

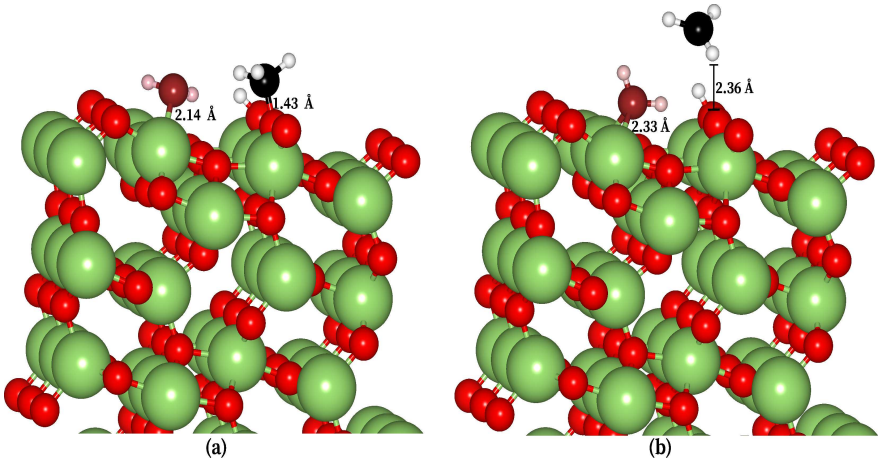

Figure 4: Optimized geometries for co-adsorption of CH_4 and H_2O on β-Ga_2O_3 (-202). (a) Dissociation of CH_4 to CH_3O_s* and H* adsorbed on adjacent surface oxygens and (b) dissociation of CH_4 to form free CH_3* and H* binds to surface O. H_2O is chemisorbed in both cases.

Furthermore, we have also investigated the interaction of CH_4 with β-Ga_2O_3 (-202) in the presence of water. The observations are tabulated in Table 4 and the schematic representation of geometries is shown in Figure 4. The spontaneous dissociation of methane remains unaffected by the presence of water. In presence of H_2O, CH_4 mostly forms a CH_3O_s* species, a representative geometry is shown in Figure 4-(a). However, in a particular case it forms a CH_3* as shown in Figure 4-(b). The CH_3-O_s bond distance is 1.44 Å and O_s-H bond

distance is 0.98 Å. Further, the H_2O molecule is activated by 3%. Thus, DFT predicts the spontaneous cleavage of C-H bond of methane on β-Ga_2O_3 (-202) catalyst in presence and absence of water.

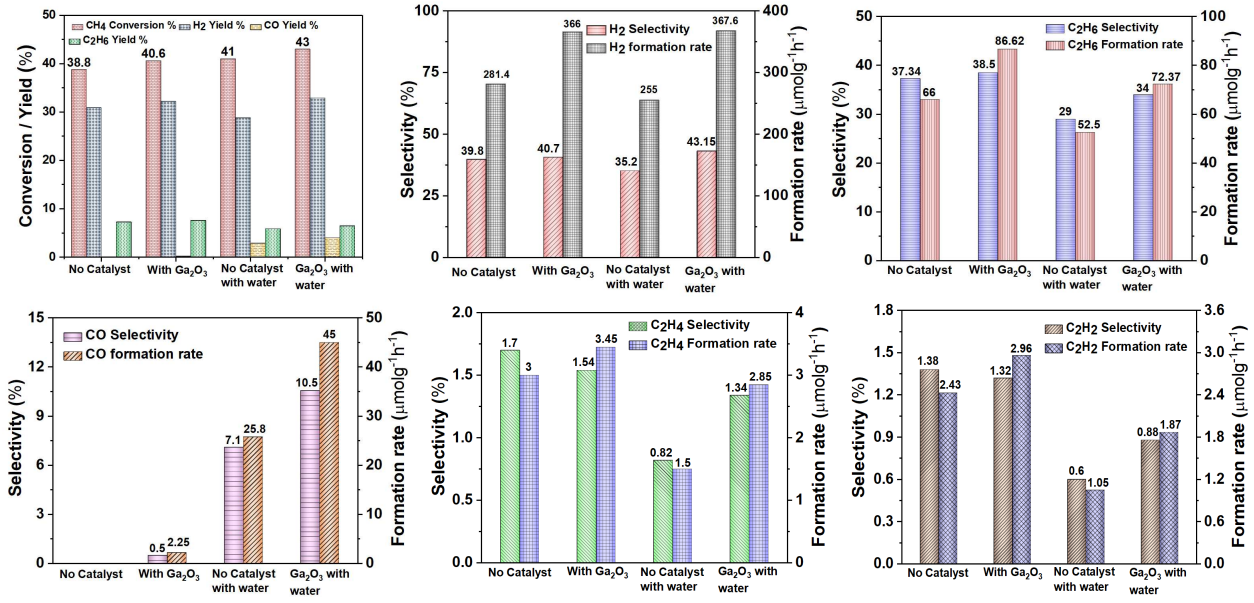

Figure 5: Details about NTP-aided reaction: (i) No catalyst (for CH_4 cracking), and (ii) with β-Ga_2O_3 catalyst (for CH_4 cracking), (iii) CH_4-H_2O reaction no catalyst, (iv) with catalyst for CH_4-H_2O reaction. Reaction conditions: catalyst weight=0.8g, CH_4 flow rate = 30 ml/min, water added = 1.5 ml, plasma temperature = near room temperature, SEI = 17.2 J/L; plasma discharge volume = 99 ml in a DBD reactor. The result discloses that β-Ga_2O_3 enhances the methane conversion, product formation rate and yield. H_2, C_2H_6, and CO are main products. These experiments explain the synergistic role of plasma-catalyst to favor product formation.

It is noted from our previous study that presence of strong basic sites would facilitate adsorption of weak acid gas like CH_4 on the surface.[6] As observed from CO_2-TPD, shown in Figure SI-6, weak and strong basic sites are located at 72.2 °C and 490 °C, respectively. Hence, β-Ga_2O_3 is a suitable candidate for CH_4 activation, also observed in DFT study. We conducted NTP experiments using β-Ga_2O_3 catalysts for methane reforming. The NTP catalysis approach is used in the DBD reactor to convert methane and methane-water mixture, and the results averaged over three runs are shown in Figure 5. It is widely recognized that a low gas flow rate helps to achieve a higher conversion because it provides the reactants with a longer residence time in the NTP environment.[22] Hence, for each experiment run, 30 ml/min of CH_4 is flown into the reactor. Plasma discharge is generated at an energy input of 17.2 J/L inside the DBD reactor. Notably, the utilization of β-Ga_2O_3 resulted in a significant

enhancement in the overall methane conversion. Without a catalyst, only 38.8% of CH_4 was converted, while with the presence of β-Ga_2O_3, the conversion increased to 40.6%, further rising to 43% with the introduction of water (refer Figure 5). Plasma-catalysis reactions undoubtedly lead to a substantial increase in formation of hydrogen. For instance, comparing the reaction without a catalyst to the reaction with a catalyst, the hydrogen formation rate increased from 281.4 $\mu molg^{-1}h^{-1}$ to 366.0 $\mu molg^{-1}h^{-1}$, representing an increase of almost 30%. Furthermore, with the plasma-β-Ga_2O_3 combination, the ethane formation rate exhibited a 31.24% increase compared to the reforming of CH_4 solely using plasma, as observed in Figure 5. However, adding water to the DBD reactor made the system unstable and decreased the yield and formation rate of C_2H_6, C_2H_4, and C_2H_2. When only H_2O is added with CH_4 in the reactor, the formation rate of H_2 reduces to 255 $\mu molg^{-1}h^{-1}$, which is lower than CH_4 alone (281.4 $\mu molg^{-1}h^{-1}$). Nevertheless, for CH_4-H_2O reaction in the presence of β-Ga_2O_3, the formation rate increases to 367.6 $\mu molg^{-1}h^{-1}$. Additionally, trace amount of CO is generated during the CH_4 reforming using β-Ga_2O_3; we postulate that the excess oxygen present on the catalyst's surface could participate in the process. Interestingly, the introduction of water to methane reforming using NTP led to higher formation rates of CO. In the presence of a β-Ga_2O_3 catalyst, the formation rate of CO with CH_4-H_2O increased by 74.42%, with 45 $\mu molg^{-1}h^{-1}$ being observed as compared to 25.8 $\mu molg^{-1}h^{-1}$ in the absence of a catalyst. The increase in formation rate of products using catalyst revealed that the strong basic sites of β-Ga_2O_3 facilitate the adsorption of CH_4 and H_2O. In our previous work, we observed spontaneous dissociation of water over β-Ga_2O_3 (111).[59] Whereas on β-Ga_2O_3 (-202), we observe spontaneous dissociation of methane. A cumulative effect of H_2O and CH_4 dissociation on (111) and (-202) facet of β-Ga_2O_3, respectively, explains the increase in formation of CO upon inclusion of water in the reaction medium. Furthermore, the other products such as C_2H_2 and C_2H_4 are observed in low quantity. Importantly, to validate that the reaction is conducted near room temperature, we used Forward Looking Infrared (FLIR) camera to monitor the inside temperature of the reactor. We found that the temperature

reached to maximum of 60°C under the reaction conditions, the corresponding temperature profile of the reaction zone confirmed the non-thermal characteristics of the DBD reactor. The temperature profile has been discussed in our previous work for the NTP-assisted steam methane reforming reaction.[6]

Table 5: We compare the present work with the existing literature for NTP-assisted conversion of methane. It is confirmed that low flow rate of methane coupled with β-Ga_2O_3 as a catalyst results in enhanced production of hydrogen. NR refers to not reported.

Reaction conditions	**Temperature**	**Methane**	**H_2**	**CO**	**C_2H_6**	**CO_2**
	°C	**conversion (%)**		**selectivity (%)**		
CH_4 + H_2O (100%) (This work)	60	41	35.2	7.1	29	Not observed
CH_4 + H_2O (100%): β-Ga_2O_3		43.0	43.15	10.5	34	
CH_4 + H_2O (100%)[6]	62	10.9	58	3.72	6.3	Not observed
CH_4 + H_2O (100%): Mn/CeO_2		17.57	62.48	4.6	1.88	
CH_4 + H_2O (100%): Cu/CeO_2		22	72.7	6.58	2.8	
CH_4 + H_2O (100%): Cu-Mn/CeO_2		14.76	50.6	5.48	2.44	
CH_4 + steam (1:3): Ni/Al_2O_3[60]	500	68	68.99	15.10	Not observed	6.09
CH_4 + H_2O (2:1)[61]	NR	45.8	100	40	0	60
CH_4: 0.5Pd/CeO_2[62]	980	23.6	50	NR	Not observed	NR
CH_4 + ∼20 % steam[21]	200	18.88	40.73	6.78	42.31	Not observed
0.3 vol.% CH_4 + 2 vol.% H_2O[23]	200	49	NR	45	NR	NR

Comparison of our research with existing literature on NTP-assisted conversion of methane is presented in Table 5. In our previous work, we have tested various flow rates viz. 50 ml/min, 80 ml/min, 110 ml/min, and 140 ml/min and the corresponding conversion was recorded to be 21.54 %, 17.4 %, 13.36 %, and 10.54 %, respectively, which shows that a low flow rate is proportional to higher methane conversion.[6] It is observed that further reducing the flow rate from 50 ml/min (previous work)[6] to 30 ml/min (current work) resulted in ∼four times higher methane conversion using plasma alone as reported in Table 5. Further, compared to previous work,[6] the selectivity towards CO and C_2H_6 is found to enhance with the presence of β-Ga_2O_3. Although Liu *et al.* reported a 100% selectivity for H_2, the yield was only 20.14%,[61] which is lower compared to the H_2 yield (30%) obtained by plasma alone

in the current work. Furthermore, they observed the reaction to be highly selective toward CO_2 (60% selectivity), whereas we did not observe CO_2 formation. While Ni/Al_2O_3 exhibits high methane conversion rates (refer to Table 5), it is associated with CO_2 formation.[60] Similarly, the use of $0.5Pd/CeO_2$ with plasma for CH_4 conversion displays higher H_2 selectivity.[62] However, it's important to note that these reactions were conducted at significantly higher temperatures (500 °C and 980 °C) compared to this work (60°C). Overall, our results demonstrate that the synergy of plasma-β-Ga_2O_3 effectively facilitates the conversion of CH_4 to H_2, CO, and C_2H_6.

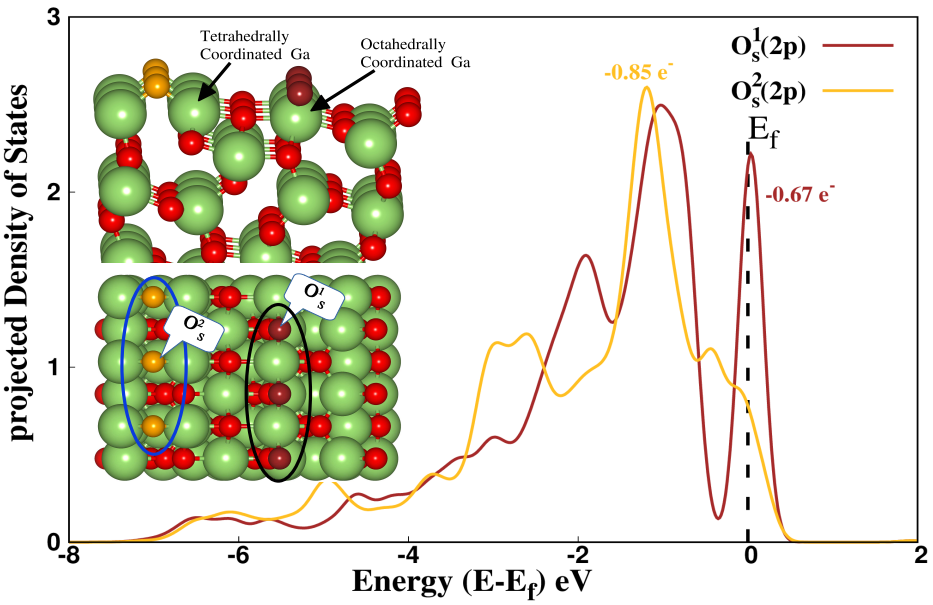

Figure 6: Site projected density of states for distinct surface oxygens on β-Ga_2O_3 (-202). Both the oxygens at the surface are co-ordinated to two Ga atoms. O^1_s:brown is co-ordinated to the octahedral Ga chain and O^2_s:golden is a part of tetrahedral Ga. O's in red belong to subsurface and does not contribute to the reactivity. Fermi energy (E_f) is set to coincide with 0 eV. Presence of sharp peak near E_f makes O^1_s site active for C-H bond cleavage.

To understand the reactivity, we investigate the electronic structure of β-Ga_2O_3 (-202) and β-Ga_2O_3 (111) surfaces. Our analysis shows that surface oxygen plays a vital role in activating the CH_4 molecule by abstracting the H atom leading to the C-H bond cleavage. To gain further insights, we investigate the site-projected density of states (*pDOS*) for O(2p). There are two unique oxygen species present at the β-Ga_2O_3 (-202) surface, which is evident from the difference in the *pDOS* shown in Figure 6. These oxygens are referred as "O^1_s" and "O^2_s" henceforth. A schematic representation of distinct surface oxygen atoms is also

shown in Figure 6, here O_s^1 is represented in brown and O_s^2 is shown in golden. The O's shown in red in Figure 6 belong to the subsurface and does not contribute to the reactivity. A sharp peak is observed at Fermi energy (E_f) for O_s^1 of magnitude almost double that of O_s^2. Both the oxygens are bi-coordinated to surface Ga atoms, however O_s^1 is coordinated to the octahedral Ga atom while O_s^2 is a part of tetrahedral chain. Hence, O_s^1 is charge deficient which is also evident from the Mulliken charges as noted in Figure 6. The Mulliken charge on O_s^1 oxygen is -0.67 e^-, while on O_s^2 it is -0.85 e^-, making O_s^1 oxygen species more electrophilic. The availability of empty states near E_f and the electrophilic nature makes O_s^1 more reactive sites for interaction with CH_4. Hence, when CH_4 is placed in the vicinity of this oxygen (i.e. O_s^1), it readily abstract a hydrogen from methane to form CH_3^* and H^*. The H atom binds to surface O_s^1 sites forming hydroxide.

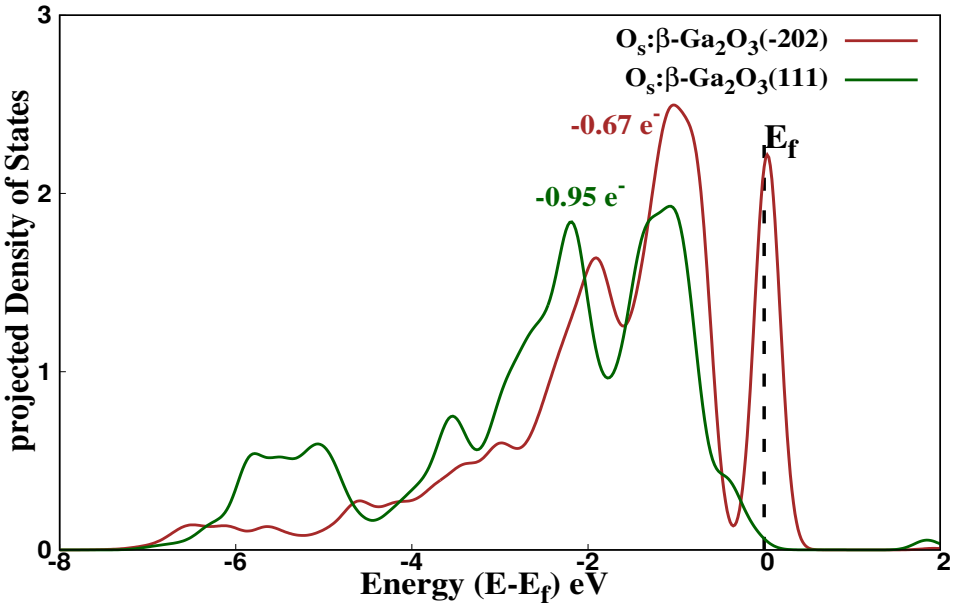

Figure 7: *pDOS* for (2p) states of surface oxygen (O_s) of β-Ga_2O_3 ($\bar{2}02$) and β-Ga_2O_3 (111). The E_f is set to coincide with 0 eV. The O_s of β-Ga_2O_3 ($\bar{2}02$) are found to be more reactive for methane activation compared to β-Ga_2O_3(111) owing to the presence of states near E_f.

Further, we observed that β-Ga_2O_3 (111) does not activate CH_4 significantly compared to β-Ga_2O_3 (-202). The correlation between states at Fermi and site specific reactivity is demonstrated in series of investigations on interaction of methanol with Zn based catalysts.[63–65] In Figure 7 we compare *pDOS* for surface oxygens of β-Ga_2O_3: (-202) and (111).

It is evident from the Figure 7, that O(2p) states are well below Fermi energy for β-Ga_2O_3 (111) while states are available at Fermi for surface oxygen of β-Ga_2O_3 (-202). This is inline with the Mulliken charges reported in Figure 7. Hence, β-Ga_2O_3 (-202) is more reactive than β-Ga_2O_3 (111).

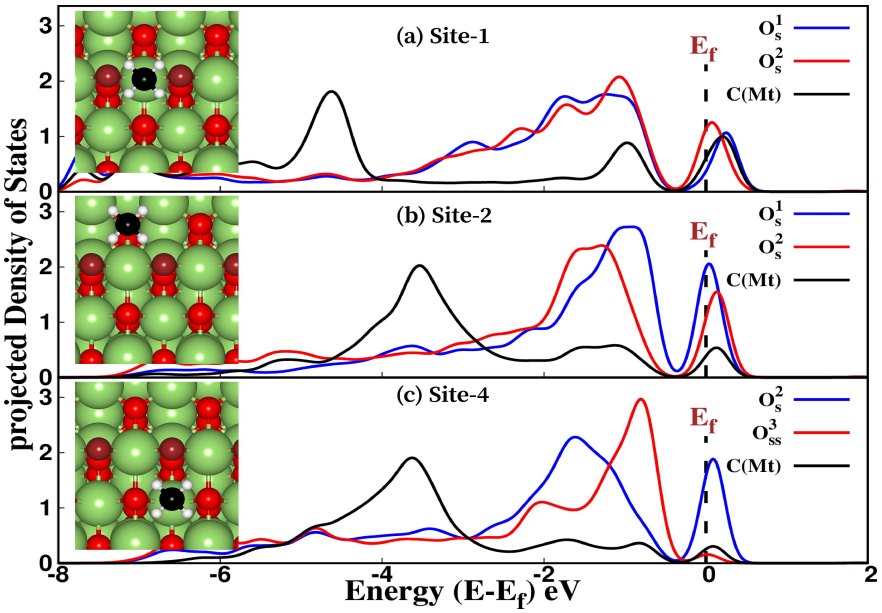

Figure 8: *pDOS* for 3 representative cases of initial geometries is reported. (a) site-1: leads to formation of CH_3O_s*, (b) site-2: formation of CH_3*, and (c) a representative case of physisorption. Fermi energy (E_f) is set to coincide with 0 eV. It is evident from the *pDOS* that significant overlap near E_f between the 2p orbitals of C and O_s leads to C-H bond dissociation in (a) and (b) where as, magnitude of overlap is minimum for (c), hence physisorption is observed. Here, O_s are surface oxygen differentiated by brown color for the aid of eyes. O_{ss} represents sub-surface oxygen and Mt represents methane molecule.

To gain further insights into what leads to the dissociation of methane to form CH_3O_s*, CH_3* or physisorption, the *pDOS* of the initial geometries corresponding to each case is investigated. In Figure 8, we plot *pDOS* for the (2p) states of the surface oxygens closest to the CH_4 molecule and the (2p) states of C in CH_4. In case (a) and (b), which lead to the formation of CH_3O_s* and CH_3*, respectively, the CH_4 molecule is in the vicinity of O_s^1, specifically at site 1 and 2 as shown in Figure SI-4(a). For the case (a), a significant overlap between the energy states of both surface oxygens and C is observed, resulting in the C-H bond cleavage and the formation of surface adsorbed CH_3O_s*. On the other hand, in case (b), the extent of overlap is less compared to case (a) and hence CH_3 does not bind to the surface oxygen instead it desorbs as methyl species. Further, for case (c), the available energy

states do not significantly overlap, resulting in physisorption of CH_4. Hence, we understand that for the dissociation of CH_4 a significant overlap between the available energy states of surface and CH_4 molecule is essential.

Table 6: We compare the NTP catalytic conversion of methane in current work with the photocatalytic conversion of methane over β-Ga_2O_3 catalysts reported in literature. Findings of this work are reported in blue. NA refers to not applicable

Catalyst	**Reaction condition**	**Gas flow rate (ml/min)**	**Reaction temperature (°C)**	**H_2 formation rate (μmolg^{-1}h^{-1})**
NA (This work)	CH_4	30	60	281.4
NA	CH_4 + H_2O			255
β-Ga_2O_3	CH_4			366
β-Ga_2O_3	CH_4 + H_2O			367.6
β-Ga_2O_3 [40]	CH_4	50	200	0.3
β-Ga_2O_3	CH_4 + H_2O			4.5
Pt(0.05)/β-Ga_2O_3	CH_4			6
Pt(0.05)/β-Ga_2O_3	CH_4 + H_2O			17.1
β-Ga_2O_3 [39]	CH_4	200 μmol batch process	37	1.45
β-Ga_2O_3 [66]	10 % CH_4/Ar	30	-	0.225
Pd(0.5)/β-Ga_2O_3			350 (in dark)	0.29
β-Ga_2O_3 [41]	10 % CH_4/Ar	30	46	0.24
Pd(0.18)-Bi(0.18)/β-Ga_2O_3				1.375

In Table 6, we present a comparison between the NTP-assisted conversion of methane (current study) and photocatalysis employing β-Ga_2O_3. The present work demonstrates that H_2 formation rate is enhanced by 30% in presence of β-Ga_2O_3 photocatalyst compared to no catalysts, as reported in Table 6. On the contrary, with only photocatalysis the H_2 formation rate is very low even with the incorporation of promoters (refer Table 6). Hence, the combined effect of NTP and β-Ga_2O_3 accelerates the conversion rate of methane to hydrogen and ethane. Since, UV light is generated during plasma reactions, there is a possibility that electron and holes pairs are produced on β-Ga_2O_3, leading to enhanced activity. Further, it is to be noted that CO_2 was not produced in the reaction. Thus, our

process can avoid vast CO_2 emissions.

Conclusion

In this study, DFT is used to investigate the interaction of methane with β-Ga_2O_3 (-202) and (111). Methane weakly interacts with (111), where as on (-202) spontaneous cleavage of the C-H bond is observed in absence and presence of water. A barrier of 0.1 eV is calculated for the formation of ethane using CI-NEB. We took these predictions further by conducting NTP-assisted methane reforming over β-Ga_2O_3, in the presence and absence of water. In a cylindrical DBD reactor, conversion of methane or reforming it in the presence of water, provide a high yield of H_2 and CO at atmospheric pressure and low temperature at specific power and flow rate. We report the conversion of methane to hydrogen and ethane along with other higher hydrocarbons, and the formation rate is enhanced in the presence of β-Ga_2O_3. CO formation is observed with the incorporation of water into the system. It is noteworthy that utilizing NTP for methane conversion does not produce CO_2. This observation is significant as it suggests the potential to circumvent CO_2 emissions in this process. Analysis of electronic signatures indicates the presence of electrophilic oxygen species on the surface of β-Ga_2O_3 (-202) which is absent on β-Ga_2O_3 (111). These electrophilic oxygen species are crucial in facilitating the spontaneous dissociation of methane on the former surface.

Conflicts of Interest

The authors declare the following financial interests/personal relationships which may be considered as potential competing interests: We have filed an application for patent based on this work.

Acknowledgement

The authors gratefully acknowledge CSIR - Fourth Paradigm Institute, CSIR - National Chemical Laboratory for the computational facility and National Supercomputing Mission (NSM) for providing computing resources of "PARAM Brahma" at IISER Pune, which is implemented by C-DAC and supported by the Ministry of Electronics and Information Technology (MeitY) and Department of Science and Technology (DST), Government of India. S.K. and A.B. thank IIT Patna for instrumental facilities. KT acknowledges CSIR for research fellowship. A.B. is immensely grateful to IIT Patna for his graduate student fellowship. Authors expresses gratitude to Aathira Nair for her critical reading and valuable suggestions.

Supporting Information Available

Supporting information is available and contains the following:

(i) Bulk: monoclinic β-Ga_2O_3. (ii) BET specific surface area of β-Ga_2O_3.

(iii) β-Ga_2O_3 (111): bare surface and after methane adsorption and pictorial representation of weakly adsorbed CH_4.

(iv) β-Ga_2O_3 (-202): bare surface with unique adsorption sites.

(v) Schematic representation of various geometries for co-adsorption of two methane molecules.

(vi) temperature programmed desorption for CO_2.

(vii) and (viii) Real time gas chromatography for methane conversion in presence and absence of water.

References

(1) Schwach, P.; Pan, X.; Bao, X. Direct conversion of methane to value-added chemicals over heterogeneous catalysts: challenges and prospects. *Chemical reviews* **2017**, *117*,

8497–8520.

(2) Huang, Z.-Q.; Zhang, T.; Chang, C.-R.; Li, J. Dynamic frustrated lewis pairs on ceria for direct nonoxidative coupling of methane. *ACS catalysis* **2019**, *9*, 5523–5536.

(3) Meng, L.; Chen, Z.; Ma, Z.; He, S.; Hou, Y.; Li, H.-H.; Yuan, R.; Huang, X.-H.; Wang, X.; Wang, X., et al. Gold plasmon-induced photocatalytic dehydrogenative coupling of methane to ethane on polar oxide surfaces. *Energy & Environmental Science* **2018**, *11*, 294–298.

(4) Wu, S.; Tan, X.; Lei, J.; Chen, H.; Wang, L.; Zhang, J. Ga-doped and Pt-loaded porous TiO_2–SiO_2 for photocatalytic nonoxidative coupling of methane. *Journal of the American Chemical Society* **2019**, *141*, 6592–6600.

(5) Bhati, M.; Dhumal, J.; Joshi, K. Lowering the C–H bond activation barrier of methane by means of SAC@Cu(111): periodic DFT investigations. *New Journal of Chemistry* **2022**, *46*, 70–74.

(6) Bajpai, A.; Mehta, S.; Joshi, K.; Kumar, S. Hydrogen from catalytic non-thermal plasma-assisted steam methane reforming reaction. *International Journal of Hydrogen Energy* **2023**, *48*, 24328–24341.

(7) Chen, L.; Qi, Z.; Zhang, S.; Su, J.; Somorjai, G. A. Catalytic hydrogen production from methane: A review on recent progress and prospect. *Catalysts* **2020**, *10*, 858.

(8) Wang, S.; Nabavi, S. A.; Clough, P. T. A review on bi/polymetallic catalysts for steam methane reforming. *International Journal of Hydrogen Energy* **2023**, *48*, 15879–15893.

(9) Jang, W.-J.; Shim, J.-O.; Kim, H.-M.; Yoo, S.-Y.; Roh, H.-S. A review on dry reforming of methane in aspect of catalytic properties. *Catalysis Today* **2019**, *324*, 15–26.

(10) Zhou, R.; Mahinpey, N. A review on catalyst development for conventional thermal

dry reforming of methane at low temperature. *The Canadian Journal of Chemical Engineering* **2023**, *101*, 3180–3212.

(11) Siang, T.; Jalil, A.; Liew, S.; Owgi, A.; Rahman, A. A review on state-of-the-art catalysts for methane partial oxidation to syngas production. *Catalysis Reviews* **2024**, *66*, 343–399.

(12) Wang, J.; Rao, Z.; Huang, Z.; Chen, Y.; Wang, F.; Zhou, Y. Recent progress of metal-oxide-based catalysts for non-oxidative coupling of methane to ethane and hydrogen. *Catalysts* **2023**, *13*, 719.

(13) Hamdan, M.; Halawy, L.; Aramouni, N. A. K.; Ahmad, M. N.; Zeaiter, J. Analytical review of the catalytic cracking of methane. *Fuel* **2022**, *324*, 124455.

(14) Meloni, E.; Martino, M.; Palma, V. A short review on Ni based catalysts and related engineering issues for methane steam reforming. *Catalysts* **2020**, *10*, 352.

(15) Hameed, S.; Comini, E. Methane conversion for hydrogen production: technologies for a sustainable future. *Sustainable Energy & Fuels* **2024**, *8*, 670–683.

(16) Wang, P.; Shi, R.; Zhao, J.; Zhang, T. Photodriven methane conversion on transition metal oxide catalyst: Recent progress and prospects. *Advanced Science* **2023**, *11*, 2305471.

(17) Liu, Z.; Xu, B.; Jiang, Y.-J.; Zhou, Y.; Sun, X.; Wang, Y.; Zhu, W. Photocatalytic conversion of methane: Current state of the art, challenges, and future perspectives. *ACS Environmental Au* **2023**, *3*, 252–276.

(18) Wu, X.; Zhang, H.; Xie, S.; Wang, Y. Photocatalytic conversion of methane: Catalytically active sites and species. *Chem Catalysis* **2023**, *3*, 100437.

(19) Nozaki, T.; Okazaki, K. Non-thermal plasma catalysis of methane: Principles, energy efficiency, and applications. *Catalysis today* **2013**, *211*, 29–38.

(20) Meng, S.; Wang, A.; He, P.; Song, H. Nonthermal plasma-assisted photocatalytic conversion of simulated natural gas for high-quality gasoline production near ambient conditions. *The Journal of Physical Chemistry Letters* **2020**, *11*, 3877–3881.

(21) ZHANG, X.; Baowei, W.; Yongwei, L.; Genhui, X. Conversion of methane by steam reforming using dielectric-barrier discharge. *Chinese Journal of Chemical Engineering* **2009**, *17*, 625–629.

(22) Kundu, S. K.; Kennedy, E. M.; Gaikwad, V. V.; Molloy, T. S.; Dlugogorski, B. Z. Experimental investigation of alumina and quartz as dielectrics for a cylindrical double dielectric barrier discharge reactor in argon diluted methane plasma. *Chemical Engineering Journal* **2012**, *180*, 178–189.

(23) Baylet, A.; Marécot, P.; Duprez, D.; Jeandel, X.; Lombaert, K.; Tatibouët, J. Synergetic effect of plasma/catalysis hybrid system for CH_4 removal. *Applied Catalysis B: Environmental* **2012**, *113*, 31–36.

(24) Kabashima, H.; Futamura, S. Continuous production of synthesis gas at ambient temperature from steam reforming of methane with nonthermal plasma. *Chemistry letters* **2002**, *31*, 1108–1109.

(25) Abiev, R. S.; Sladkovskiy, D. A.; Semikin, K. V.; Murzin, D. Y.; Rebrov, E. V. Nonthermal plasma for process and energy intensification in dry reforming of methane. *Catalysts* **2020**, *10*, 1358.

(26) Mei, D.; Zhu, X.; Wu, C.; Ashford, B.; Williams, P. T.; Tu, X. Plasma-photocatalytic conversion of CO_2 at low temperatures: Understanding the synergistic effect of plasma-catalysis. *Applied Catalysis B: Environmental* **2016**, *182*, 525–532.

(27) Feng, J.; Sun, X.; Li, Z.; Hao, X.; Fan, M.; Ning, P.; Li, K. Plasma-assisted reforming of methane. *Advanced Science* **2022**, *9*, 2203221.

(28) Bajpai, A.; Kumar, S. Nonthermal plasma-assisted CO_2-H_2O conversion over NiO and Co_3O_4 supported on CeO_2. *Chemical Engineering & Technology* **2023**, *46*, 1485–1493.

(29) Bajpai, A.; Kumar, S. Tailoring the surface acidity of catalyst to enhance nonthermal plasma-assisted ammonia synthesis rates. *Molecular Catalysis* **2024**, *557*, 113961.

(30) Chung, W.-C.; Tsao, I.-Y.; Chang, M.-B. Novel plasma photocatalysis process for syngas generation via dry reforming of methane. *Energy Conversion and Management* **2018**, *164*, 417–428.

(31) Alioui, O.; Badawi, M.; Erto, A.; Amin, M. A.; Tirth, V.; Jeon, B.-H.; Islam, S.; Balsamo, M.; Virginie, M.; Ernst, B., et al. Contribution of DFT to the optimization of Ni-based catalysts for dry reforming of methane: a review. *Catalysis Reviews* **2023**, *65*, 1468–1520.

(32) Huang, E.; Liu, P. Theoretical Perspective of Promoting Direct Methane-to-Methanol Conversion at Complex Metal Oxide–Metal Interfaces. *The Journal of Physical Chemistry Letters* **2023**, *14*, 6556–6563.

(33) Senanayake, S. D.; Rodriguez, J. A.; Weaver, J. F. Low temperature activation of methane on metal-oxides and complex interfaces: Insights from surface science. *Accounts of Chemical Research* **2020**, *53*, 1488–1497.

(34) Wang, C.-C.; Siao, S. S.; Jiang, J.-C. C–H bond activation of methane via σ–d interaction on the IrO_2(110) surface: density functional theory study. *The Journal of Physical Chemistry C* **2012**, *116*, 6367–6370.

(35) Liang, Z.; Li, T.; Kim, M.; Asthagiri, A.; Weaver, J. F. Low-temperature activation of methane on the IrO_2(110) surface. *Science* **2017**, *356*, 299–303.

(36) Kwon, G.; Shin, D.; Jeong, H.; Sahoo, S. K.; Lee, J.; Kim, G.; Choi, J.; Kim, D. H.;

Han, J. W.; Lee, H. Oxidative methane conversion to ethane on highly oxidized Pd/CeO_2 catalysts below 400° C. *ChemSusChem* **2020**, *13*, 677–681.

(37) Liu, S.; Udyavara, S.; Zhang, C.; Peter, M.; Lohr, T. L.; Dravid, V. P.; Neurock, M.; Marks, T. J. "Soft" oxidative coupling of methane to ethylene: Mechanistic insights from combined experiment and theory. *Proceedings of the National Academy of Sciences* **2021**, *118*, e2012666118.

(38) Amano, F.; Ishimaru, M. Hydroxyl radical formation on metal-loaded Ga_2O_3 photocatalysts for dehydrogenative coupling of methane to ethane with water. *Energy & Fuels* **2022**, *36*, 5393-5402.

(39) Yuliati, L.; Itoh, H.; Yoshida, H. Photocatalytic conversion of methane and carbon dioxide over gallium oxide. *Chemical Physics Letters* **2008**, *452*, 178–182.

(40) Shimura, K.; Yoshida, T.; Yoshida, H. Photocatalytic activation of water and methane over modified gallium oxide for hydrogen production. *The Journal of Physical Chemistry C* **2010**, *114*, 11466–11474.

(41) Singh, S. P.; Yamamoto, A.; Fudo, E.; Tanaka, A.; Kominami, H.; Yoshida, H. A Pd-Bi dual-cocatalyst-loaded gallium oxide photocatalyst for selective and stable nonoxidative coupling of methane. *ACS Catalysis* **2021**, *11*, 13768–13781.

(42) Ishimaru, M.; Amano, F.; Akamoto, C.; Yamazoe, S. Methane coupling and hydrogen evolution induced by palladium-loaded gallium oxide photocatalysts in the presence of water vapor. *Journal of Catalysis* **2021**, *397*, 192–200.

(43) Wen, J.-H.; Wang, G.-C. Methane nonoxidative direct conversion to C2 hydrogenations over CeO_2-supported Pt catalysts: A density functional theory study. *The Journal of Physical Chemistry C* **2020**, *124*, 13249–13262.

(44) Zhang, W.; Fu, C.; Low, J.; Duan, D.; Ma, J.; Jiang, W.; Chen, Y.; Liu, H.; Qi, Z.; Long, R., et al. High-performance photocatalytic nonoxidative conversion of methane to ethane and hydrogen by heteroatoms-engineered TiO_2. *Nature Communications* **2022**, *13*, 2806.

(45) Yin, F.; Li, M.-R.; Wang, G.-C. Periodic density functional theory analysis of direct methane conversion into ethylene and aromatic hydrocarbons catalyzed by Mo_4C_2/ZSM-5. *Physical Chemistry Chemical Physics* **2017**, *19*, 22243–22255.

(46) (a) Blöchl, P. E. Projector augmented-wave method. *Physical Review B* **1994**, *50*, 17953–17979; (b) Kresse, G.; Joubert, D. From ultrasoft pseudopotentials to the projector augmented-wave method. *Physical Review B* **1999**, *59*, 1758–1775.

(47) (a) Perdew, J. P.; Burke, K.; Ernzerhof, M. Generalized Gradient Approximation Made Simple. *Physical Review Letters* **1996**, *77*, 3865–3868; (b) Perdew, J. P.; Burke, K.; Ernzerhof, M. Generalized Gradient Approximation Made Simple [Phys. Rev. Lett. 77, 3865 (1996)]. *Physical Review Letters* **1997**, *78*, 1396–1396.

(48) (a) Kresse, G.; Hafner, J. *Ab initio* molecular-dynamics simulation of the liquid-metal–amorphous-semiconductor transition in germanium. *Physical Review B* **1994**, *49*, 14251–14269; (b) Kresse, G.; Furthmüller, J. Efficient iterative schemes for *ab initio* total-energy calculations using a plane-wave basis set. *Physical Review B* **1996**, *54*, 11169–11186; (c) Kresse, G.; Furthmüller, J. Efficiency of ab-initio total energy calculations for metals and semiconductors using a plane-wave basis set. *Computational Material Science* **1996**, *6*, 15–50.

(49) Grimme, S. Semiempirical GGA-type density functional constructed with a long-range dispersion correction. *Journal of computational chemistry* **2006**, *27*, 1787–1799.

(50) Jain, A.; Ong, S. P.; Hautier, G.; Chen, W.; Richards, W. D.; Dacek, S.; Cholia, S.;

Gunter, D.; Skinner, D.; Ceder, G.; Persson, K. a. The Materials Project: A materials genome approach to accelerating materials innovation. *APL Materials* **2013**, *1*, 011002.

(51) Geller, S. Crystal structure of β-Ga_2O_3. *The Journal of Chemical Physics* **1960**, *33*, 676–684.

(52) Stradi, D.; Jelver, L.; Smidstrup, S.; Stokbro, K. Method for determining optimal supercell representation of interfaces. *Journal of Physics: Condensed Matter* **2017**, *29*, 185901.

(53) Henkelman, G.; Uberuaga, B. P.; Jónsson, H. A climbing image nudged elastic band method for finding saddle points and minimum energy paths. *The Journal of chemical physics* **2000**, *113*, 9901–9904.

(54) (a) Dronskowski, R.; Blöchl, P. E. Crystal orbital Hamilton populations (COHP): energy-resolved visualization of chemical bonding in solids based on density-functional calculations. *The Journal of Physical Chemistry* **1993**, *97*, 8617–8624; (b) Deringer, V. L.; Tchougréeff, A. L.; Dronskowski, R. Crystal orbital Hamilton population (COHP) analysis as projected from plane-wave basis sets. *The Journal of Physical Chemistry A* **2011**, *115*, 5461–5466; (c) Maintz, S.; Deringer, V. L.; Tchougréeff, A. L.; Dronskowski, R. Analytic projection from plane-wave and PAW wavefunctions and application to chemical-bonding analysis in solids. *Journal of Computational Chemistry* **2013**, *34*, 2557–2567; (d) Maintz, S.; Deringer, V. L.; Tchougréeff, A. L.; Dronskowski, R. LOBSTER: A tool to extract chemical bonding from plane-wave based DFT. *Journal of Computational Chemistry* **2016**, *37*, 1030–1035.

(55) Pearton, S.; Yang, J.; Cary IV, P. H.; Ren, F.; Kim, J.; Tadjer, M. J.; Mastro, M. A. A review of Ga_2O_3 materials, processing, and devices. *Applied Physics Reviews* **2018**, *5*, 011301.

(56) Xiao, H.-D.; Ma, H.-L.; Xue, C.-S.; Zhuang, H.-Z.; Ma, J.; Zong, F.-J.; Zhang, X.-J.

Synthesis and structural properties of beta-gallium oxide particles from gallium nitride powder. *Materials chemistry and physics* **2007**, *101*, 99–102.

(57) Ojha, N.; Metya, A. K.; Kumar, S. Influence of plasmonic metals (Ag, Cu) on overall CO_2 photoreduction activity of β-Ga_2O_3. *Applied Surface Science* **2022**, *580*, 152315.

(58) Chaudhari, V.; Dutta, K.; Li, C.-J.; Kopyscinski, J. Mechanistic insights of methane conversion to ethylene over gallium oxide and gallium nitride using density functional theory. *Molecular Catalysis* **2020**, *482*, 110606.

(59) Ojha, N.; Thakkar, K.; Bajpai, A.; Joshi, K.; Kumar, S. Photoinduced CO_2 and N_2 reductions on plasmonically enabled gallium oxide. *Journal of Colloid and Interface Science* **2023**, *629*, 654–666.

(60) Kim, S. S.; Jorat, M.; Voecks, G.; Kuthi, A.; Surampudi, S.; Kent, R. L. Hydrogen from steam methane reforming by catalytic nonthermal plasma using a dielectric barrier discharge reactor. *AIChE Journal* **2020**, *66*, e16880.

(61) Liu, Q.; Zheng, H.; Yang, R.; Pan, G. Experimental study on chemical recuperation using hybrid dielectric barrier discharge-catalytic methane-steam reforming. *Proceedings of the Institution of Mechanical Engineers, Part A: Journal of Power and Energy* **2014**, *228*, 451–461.

(62) Hu, X.; Liu, Y.; Dou, L.; Zhang, C.; Zhang, S.; Gao, Y.; Tu, X.; Shao, T. Plasma enhanced anti-coking performance of Pd/CeO 2 catalysts for the conversion of methane. *Sustainable Energy & Fuels* **2022**, *6*, 98–109.

(63) Mehta, S.; Joshi, K. From molecular adsorption to decomposition of methanol on various ZnO facets: A periodic DFT study. *Applied Surface Science* **2022**, *602*, 154150.

(64) Mehta, S.; Joshi, K. Electronic fingerprints for diverse interactions of methanol with various Zn-based systems. *Surface Science* **2023**, *736*, 122350.

(65) Mehta, S.; Agarwal, S.; Kenge, N.; Mekala, S. P.; Patil, V.; Raja, T.; Joshi, K. Mixed metal oxide: A new class of catalyst for methanol activation. *Applied Surface Science* **2020**, *534*, 147449.

(66) Singh, S. P.; Anzai, A.; Kawaharasaki, S.; Yamamoto, A.; Yoshida, H. Non-oxidative coupling of methane over Pd-loaded gallium oxide photocatalysts in a flow reactor. *Catalysis Today* **2021**, *375*, 264–272.